



Article

# Microsegregation Model Including Convection and Tip Undercooling: Application to Directional Solidification and Welding

Thomas Billotte <sup>1,2</sup>, Dominique Daloz <sup>1,2,\*</sup> , Bernard Rouat <sup>1,2</sup>, Guillaume Tirand <sup>3</sup>,  
Jacob R. Kennedy <sup>1,2</sup>, Vincent Robin <sup>4</sup> and Julien Zollinger <sup>1,2</sup> 

<sup>1</sup> Department of Metallurgy and Materials Science and Engineering, Institut Jean Lamour, UMR CNRS 7198, Université de Lorraine, 54000 Nancy, France; t.billotte@isgroupe.com (T.B.); bernard.rouat@univ-lorraine.fr (B.R.); jacob-roman.kennedy@univ-lorraine.fr (J.R.K.); julien.zollinger@univ-lorraine.fr (J.Z.)

<sup>2</sup> Laboratory of Excellence on Design of Alloy Metals for Low-mAss Structures ('LabEx DAMAS'), Université de Lorraine, 57073 Metz, France

<sup>3</sup> AREVA, Technical Center, 71100 Saint-Marcel, France; guillaume.tirand@framatome.com

<sup>4</sup> AREVA, Engineering & Projects, 69006 Lyon, France; vincent.robin@edf.fr

\* Correspondence: dominique.daloz@univ-lorraine.fr; Tel.: +33-372-742-669

Received: 29 June 2018; Accepted: 15 July 2018; Published: 20 July 2018



**Abstract:** The microsegregation behavior of alloy filler metal 52 (FM 52) was studied using microprobe analysis on two different solidification processes. First, microsegregation was characterized in samples manufactured by directional solidification, and then by gas tungsten arc welding (GTAW). The experimental results were compared with Thermo-Calc calculations to verify their accuracy. It was confirmed that the thermodynamic database predicts most alloying elements well. Once this data had been determined, several tip undercooling calculations were carried out for different solidification conditions in terms of fluid flow and thermal gradient values. These calculations allowed the authors to develop a parametrization card for the constants of the microsegregation model, according to the process parameters (e.g., convection in melt pool, thermal gradient, and growth velocity). A new model of microsegregation, including convection and tip undercooling, is also proposed. The Tong–Beckermann microsegregation model was used individually and coupled with a modified Kurz–Giovanola–Trivedi (KGT) tip undercooling model, in order to take into account the convection in the fluid flow at the dendrite tip. Model predictions were compared to experimental results and showed the microsegregation evolution accurately.

**Keywords:** microsegregation; gas tungsten arc welding; directional solidification; FM52 filler metal; ERNiCrFe-7; tip undercooling

## 1. Introduction

The first pressurized water reactor (PWR) components were manufactured from stainless steel and nickel A600 alloys. Welding of the reactors was performed using FM82 filler metal in order to maintain both mechanical and anti-corrosion properties. Since 1990, A690 nickel alloy has replaced the A600 alloy in order to improve stress corrosion cracking resistance [1]. In addition, a new filler metal, FM52, was developed. A690 alloy mainly consists of an austenitic matrix containing  $M_{23}C_6$  (MC) carbides [2–4]. MC carbides are also observed in the filler metal FM52 [5–7], as well as some titanium nitrides, as reported in the literature [8,9].

A690 and FM52 satisfy the specification for corrosion resistance [10], but suffer from a tendency for ductility dip cracking (DDC) during welding [11–17]. Different factors may affect the DDC

sensitivity, such as alloy composition, element segregation (phosphorous and sulfur), secondary phase precipitation at grain boundaries, grain boundary sliding, or grain boundary orientation [12]. Since 2000, this has led to many developments to improve the DCC resistance, focusing mainly on the chemical composition [18]. FM52 can now be reinforced using boron and zirconium for FM52M [19], and using molybdenum and niobium for FM52MSS, to improve its mechanical properties [20,21]. However, segregation of boron at the grain boundaries promotes the formation of low melting point compounds, generating liquation cracks [22]. This cracking behavior can be further exacerbated by the presence of oxide bifilms [23]; the same effect is noted for zirconium [24]. The importance of back-diffusion to reduce solidification cracking has also recently been shown [25], along with the fact that microsegregation in gas tungsten arc welding (GTAW) can be somewhat controlled by the use of pulsed current [26]. It is critical then, for development and application, to thoroughly understand how segregation occurs and how to model it. It is useful to simulate solidification structures using a model in which a cellular automaton is coupled with a finite element mesh (CAFE) [27,28].

When such predictive modeling tools are applied to welding or additive manufacturing, the Scheil rule (or truncated Scheil [29])—based on the hypothesis that no solid diffusion occurs—is employed, due to the relatively rapid solidification compared to other casting processes [30]. Time allowed for back-diffusion in the solid is low in rapid solidification, which correlates well with the Scheil model hypothesis. However, the structures formed are much finer than those obtained with slower solidification processes. This means that less time is needed for elements to back-diffuse into the solid and, thus, the applicability of the Scheil rule becomes more problematic [31]. Additionally, the intense convection that occurs in the weld pool may affect the solutal build-up associated with solidification, and thereby modify the dendrite tip undercooling. This is not taken into account in the Scheil description, and may affect the initial conditions for microsegregation.

Currently, there is no published work which specifically regards dendrite tip undercooling and convection in the melt pool [32]. Convection is in the order of tens of centimeters per second during welding. Thus, it is relevant to quantify the convection effect on undercooling and include it in a microsegregation model. The ability of the Scheil model to correctly represent the microsegregation in such rapid growth conditions may also be investigated. This paper will address both of these points.

In this work, quenched directional solidification (QDS) and gas tungsten arc welding (GTAW) of FM52 were carried out. From the experiments, the microsegregation was characterized. A KGT [33] tip undercooling model—which took fluid flow into account [34]—was applied, in order to quantify the importance of convection on the undercooling. The Tong–Beckermann [35] microsegregation model was also used, which could account for the importance of back-diffusion. This model, together with the classical lever rule and Gulliver–Scheil model, are compared with the experimental results. These results are discussed, and rules for better use of microsegregation models are proposed.

## 2. Experimental Section

The FM52 alloy was provided by AREVA. The chemical composition of the alloy was measured using the electron probe micro-analysis (EPMA) on a JEOL JXA 8530F apparatus (JEOL, Tokyo, Japan). Table 1 shows the results of this analysis, compared with the manufacturer’s specifications.

**Table 1.** Composition of alloy filler metal 52 (FM52) in weight percent.

	Ni	Cr	Fe	Al	Ti	Mn	Si	C
EPMA	57.98	29.98	10.06	0.65	0.52	0.29	0.13	0.03
Specification [36]	≈60	28–31.5	7–11	<1.1	<1	<0.5	<0.5	<0.04

The solidus and liquidus temperatures were determined using a SETARAM Setsys 16/18 differential thermal analysis (DTA) (SETARAM, Lyon, France). Four cooling and heating rates were applied, ranging from 2 to 20 K/min. The results were examined using the Boettinger [37]

recommendations and the Bobadilla observations [38]. The DTA results for solidus and liquidus temperatures are summarized in Table 2, and compared with thermodynamic calculations performed using the Thermo-Calc software (Thermo-Calc 2018b, Thermo-Calc software, Solna, Sweden) with the TTNi8 database [39]. The solidification range ( $\Delta T_0$ ) found by DTA analysis was 10.6 °C, which is very close to the value (13 °C) found by Wu and Tsai [40]. As seen in Table 2, the values given by the TTNi8 database for the FM52 alloy (considering all alloying elements) does not reflect the experimental DTA measurements, especially for the solidification range (36 °C vs. 10.6 °C). If only the major constituent elements of the alloy are considered (Cr, Fe), the calculated solidification range is 8.4 °C, showing much better agreement with the DTA measurements.

**Table 2.** Results of the differential thermal analyses (DTA) and thermodynamic calculations with the TTNi8 database.

	DTA (°C)	Thermo-Calc (°C, FM52)	Thermo-Calc (°C, Ni-29.98Cr-10.06Fe)
Solidus	1379.2	1364	1409.4
Liquidus	1389.8	1400	1417.8

Experiments involving quenching during directional solidification (QDS) were performed with a specially designed Bridgman type furnace. This method allows the thermal gradient ( $G$ ) and the solidification velocity ( $V$ ) to be controlled independently. The quench imposes a cooling rate of 100 °C/s, and is able to freeze the microstructure and microsegregations during solidification [41,42]. Alloy FM52 was melted and cast into cylindrical rods, 5 mm in diameter, which were used in the Bridgman furnace. After the QDS experiments, transverse cross-sections were cut along the length of the mushy zone. Each section corresponds to a given temperature before the quench and, for a given solid fraction, the morphology and the amount of segregation in the solidifying alloy.

The welding experiments were performed using gas tungsten arc welding (GTAW) under argon. The filler metal was FM52 alloy and the welding plates were A690 nickel alloy. Contrary to the QDS experiments, the solidification operating parameters are not controlled in the GTAW process. For this study, the growth velocity was considered equal to the welding speed, and the thermal gradient was determined using the SYSWELD software (2017, ESI, Paris, France). The solidification parameters, and  $G$  and  $V$  for the QDS and welding experiments are given in Table 3.

**Table 3.** Solidification parameters used in the quenched directional solidification (QDS) and welding experiments.

Test Type	Thermal Gradient (K/m)	$V$ (mm/s)	$G/V$ (K·s/m <sup>2</sup> )	$G \cdot V$ (K/s)
QDS	5300	0.09	$5.89 \times 10^7$	0.477
		0.03	$1.77 \times 10^8$	0.159
		0.013	$4.08 \times 10^8$	0.0689
	3000	0.09	$3.33 \times 10^7$	0.27
		0.03	$1 \times 10^8$	0.09
		0.013	$2.31 \times 10^8$	0.039
GTAW	$\approx 300,000$	1.66	$1.81 \times 10^8$	498

To characterize microsegregation, EPMA measurements were performed using regular analysis grids [41–44]. The parameters for the systematic sampling were determined using a previously developed method [44]. The dimensions of the analysis grids were the same for all the analyzed samples, e.g., 196 measurements with a 100  $\mu\text{m}$  step size, so that the sampling parameter,  $r$ , defined by  $r = \frac{\text{step}}{\lambda_1}$ , was always less than or equal to 10 [44].

The sorting strategy used was based on the element which was known to have the greatest tendency to segregate in the liquid [41]. In this work, titanium was selected, as Ti is known to segregate

in the liquid during solidification [9]. All other elements were arranged following the Ti values in ascending order. In order to compare them, the microsegregation profiles were normalized to the mean composition calculated from all 196 points.

### 3. Microstructure and Microsegregation

#### 3.1. Secondary Dendrite Arm Spacing (SDAS) Law

The scale of microsegregation was found using secondary dendrite arm spacing (SDAS) measurements. It was necessary to know the SDAS evolution, with respect to the solidification parameters, in order to utilize the data in the Tong–Beckermann (TB) model. For this reason, several QDS experiments were performed with different solidification conditions. For each experiment, several micrographs from the longitudinal section of the QDS samples were taken to measure the SDAS. This was also carried out for the GTAW experiments.

Figure 1 illustrates the different sizes of the solidification structures from the experiments. As shown in Figure 1a, the solidification front is clearly visible on the QDS micrographs (Figure 1a–c). The dendrites grow following the thermal gradient, however, in the case of GTAW, it was less clear, since the thermal gradient vector was not constant. Nevertheless, a dendritic structure can still be observed in Figure 1d. The evolution of the size of the solidification structures is also visible in Figure 1. As the product of  $G$  and  $V$  increased, the size of the structures decreased, as can be seen by comparing the QDS experiments. This is even more evident with the GTAW experiments, where the cooling rate is 1000 times higher than the maximum cooling rate obtained with QDS.

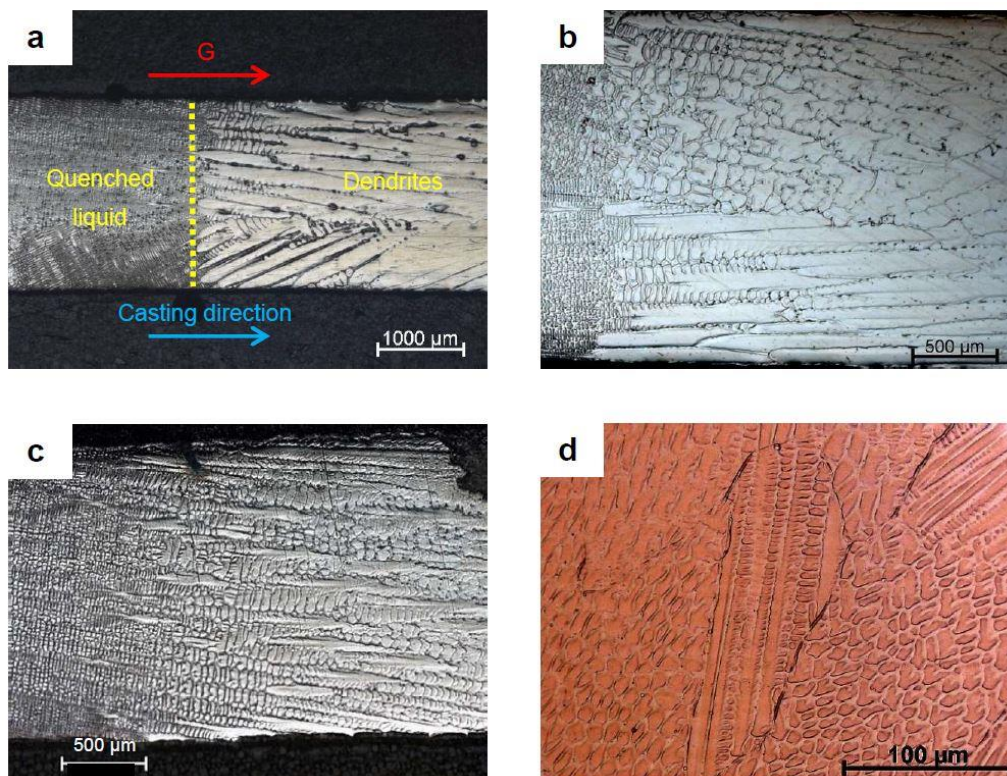


**Figure 1.** Micrographs for the secondary dendrite arm spacing (SDAS) measurement after electrolytic etching, using a 10 g  $\text{H}_2\text{C}_2\text{O}_4$  with 100 mL  $\text{H}_2\text{O}$  reagent, under the applied potential 4 V DC for 30–40 s: (a) QDS for a solidification velocity  $V = 0.013$  mm/s and thermal gradient ( $G$ ) = 3000 K/m; (b) QDS for  $V = 0.03$  mm/s and  $G = 5300$  K/m; (c) QDS for  $V = 0.09$  mm/s and  $G = 5300$  K/m; and (d) gas tungsten arc welding (GTAW).



This data was supplemented by the measurements of Blecher et al. [45] in an A690 alloy, which had a composition very similar to the FM52 alloy. The SDAS evolution, with respect to the cooling rate, is plotted in Figure 2, using the Frenk and Kurz method [46]. The equation of the fitted curve, presented as a dashed line in Figure 2, is given by Equation (1). This law is very similar to the Blecher et al. law [45], and is very close to the well-known SDAS law for metallic alloys,  $\lambda_2 = A \times (G \times V)^{\frac{1}{3}}$ , where A is a material constant [47].

$$\lambda_2 = 23.92 \times (G \times V)^{-0.323} \text{ in microns.} \quad (1)$$

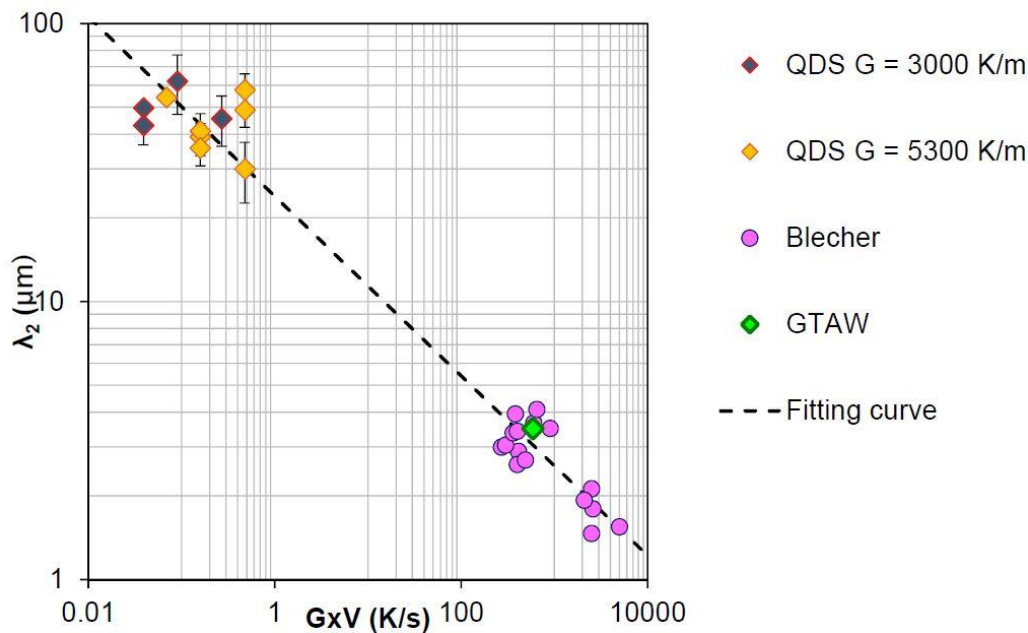


**Figure 2.** SDAS evolution of FM52 alloy as function of the cooling rate in K/s for QDS, GTAW experiments and Blecher et al.'s [45] measurements.

### 3.2. Microsegregation Results

The microsegregation profiles for the QDS and GTAW experiments are given for Fe, Cr, Ti and Al in Figure 3. Even though the cooling rate was a thousand times larger in QDS than GTAW, the microsegregation profiles do not differ significantly. In fact, they are identical for all elements (Figure 3), despite the cooling rates differing by three orders of magnitude.

The trends in the segregations shown in Figure 3 are comparable to others reported for different nickel alloys containing chromium, titanium and aluminum [48,49]. These elements segregate in the liquid during solidification, as opposed to iron which does not.

Two methods of estimating the partition coefficient were considered. From the phase diagram, the partition coefficient, denoted  $k_1$  in the following, was estimated using Equation (2). QDS offers a second possibility of estimating the partition coefficient if the microsegregation is analyzed on a transverse section, where the solid fraction is less than 1. This method was used to calculate the partition coefficient, denoted  $k_2$ , defined in Equation (3). The second method was interesting as it was able to evaluate the influence of the composition at the interface and the temperature on the partition coefficient.

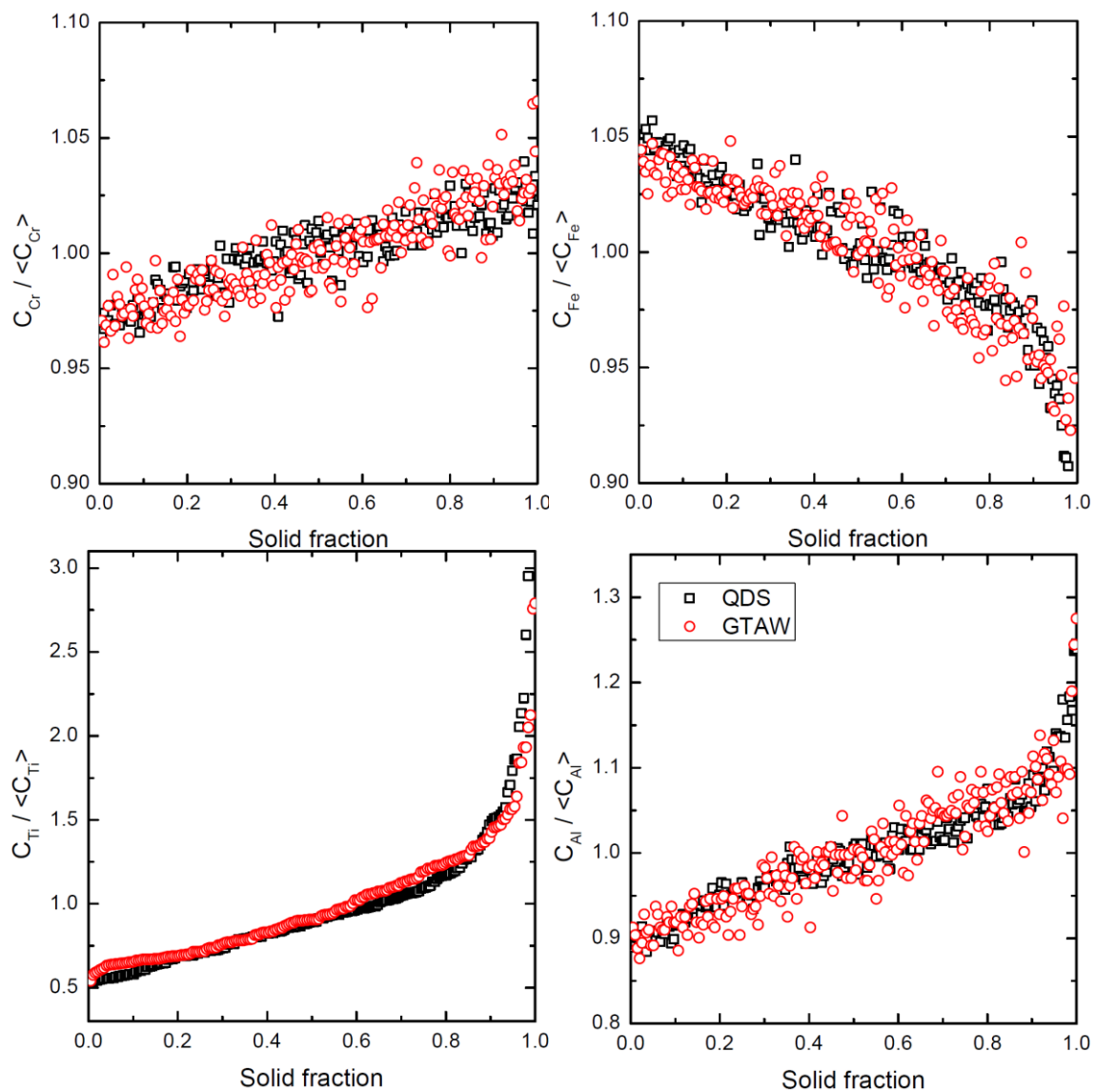


**Figure 3.** Comparison of microsegregation profiles between QDS,  $GV = 0.477$  K/s and GTAW experiments.

Due to the small solidification range of the FM52 alloy, the length of the mushy zone was only  $\sim 2$  mm. It was therefore difficult to accurately cut. Nevertheless, it was successfully sectioned on the QDS test for  $GV = 0.039$  K/s. In the analyzed region, the solid fraction was estimated to be approximately 80%.

$$k_1 = \frac{\text{Solid composition for } f_s = 0}{\text{Mean composition}} \quad (2)$$

$$k_2 = \frac{\text{Solid composition at quench moment}}{\text{Mean composition of quenched liquid}} \quad (3)$$

The values of the partition coefficients are presented in Table 4. Over three cooling rates and two solid fractions, the values did not have significant variation. This indicates that the partition coefficients do not depend on the composition and temperature changes at the interface.

**Table 4.** Partition coefficients QDS, GTAW, and Thermo-Calc calculations.

	<i>k</i>	Cr	Fe	Al	Ti	Mn	Si
QDS, GV = 0.477 K/s	<i>k</i> <sub>1</sub>	0.96	1.05	0.87	0.5	0.75	0.59
QDS, GV = 0.16 K/s	<i>k</i> <sub>1</sub>	0.96	1.07	0.86	0.46	0.73	0.66
QDS, GV = 0.039 K/s	<i>k</i> <sub>1</sub>	0.98	1.06	0.87	0.5	0.76	0.66
	<i>k</i> <sub>2</sub>	0.98	1.05	0.94	0.62	0.71	0.59
GTAW	<i>k</i> <sub>1</sub>	0.97	1.04	0.91	0.54	x	x
Thermo-Calc for FM52 alloy	<i>k</i> <sub>1</sub>	0.93	1.13	0.99	0.41	0.54	0.62
Thermo-Calc for ternary Ni-29.98Cr-10.06Fe	<i>k</i> <sub>1</sub>	0.92	1.11	x	x	x	x

The experimental analysis was concluded with partition coefficients determined for alloy FM52 and the ternary alloy approximation from the thermodynamic TTNi8 database. The small effect of composition on the majority element partition coefficients should be noted. The data for the ternary and FM52 alloys were similar. The values presented in Table 4 differ somewhat between the measured and calculated. In the Thermo-Calc computation, the undercooling was not considered, so the first solid that formed had the same composition as was predicted by the phase diagram, i.e., the product between the nominal composition and the partition coefficient. These results supported the assumption that the FM52 alloy behaved like the considered ternary alloy, as was assumed for the following model.

In addition to the thermodynamic data, the most surprising result was that the microsegregation profiles were identical in QDS and GTAW, which could not be explained by a size effect (Fourier number was of the order of 0.3 in QDS, compared to 0.025 in GTAW). Several factors had to be considered in order to explain this. First, it was necessary to clarify the role of convection (important in welding) on undercooling, and by extension on microsegregation. Next, attention had to be paid to the size of the structures and to the experimental determination of the microsegregation. These two questions were not considered by Liang and Chen [50].

#### 4. Modelling Microsegregation: Including Fluid Flow

##### 4.1. Microsegregation Model

The most common microsegregation models are the well-known lever rule and Scheil model [51]. The lever rule assumes an infinite diffusion in both the liquid and the solid phases, while the Scheil model assumes no diffusion in the solid phase and infinite diffusion in the liquid phase. They are usually used to evaluate the possible microsegregation range, but cannot be considered fully realistic. Many more elaborate microsegregation models have been proposed over the years, most based on the Clyne–Kurz (CK) model [52], the Kobayashi model [53], the Wang–Beckermann model [54] or the Tong–Beckermann (TB) model [35]. In the present work, only the TB model was considered.

Compared to the Scheil model, the TB model accounts for solute diffusion in the solid phase, through a solutal Fourier number,  $\alpha$ , defined in the CK model as [52]:

$$\alpha_i = \frac{D_i^s t_f}{\lambda_2^2} \quad (4)$$

where  $D_i^s$  is the diffusion coefficient for the solute  $i$  in the solid phase,  $t_f$  is the local solidification time, defined as  $\Delta T_0 / G_T V$ , and  $\lambda_2$  is the secondary dendrite arm spacing.  $\alpha$  is also known as the back-diffusion parameter.

In addition to the CK model, the TB model considers limited diffusion both into the solid and liquid phase, which can be relevant when the solidification velocity is important, such as is the case in welding operations. Similar to the CK model, the TB model introduces a solutal Fourier number  $\beta$  for diffusion in the liquid phase:

$$\beta = \frac{D_i^l t_f}{\lambda_2^2} \quad (5)$$

where  $D_i^l$  is the solute diffusion coefficient in the liquid phase. This Fourier number may also be used to define a second adimensional parameter called  $\beta'$ , introducing a "tuning constant",  $\sigma$ , defined as:

$$\beta' = \sigma\beta. \quad (6)$$

This constant is included in the model to compensate for the error introduced by the solute diffusion of the moving solid/liquid interface, which does not satisfy the zero flux condition at the symmetry line separating two dendrites [35]. In practical terms, this tuning constant accounts for the dendrite tip undercooling and changes the composition of the first solid, accordingly. The microsegregation evolution during solidification can be obtained by solving the following differential equation for solid fraction  $f_s$  ranging from 0 to 1:

$$\frac{2\beta' f_s}{k_i} (1 - \delta) \frac{dw_i^{s*}}{df_s} = (1 + 6\alpha) (w_i^0 - w_i^{s*}) + \left( \frac{w_i^{s*}}{k_i} - w_i^0 \right) \left( \frac{\delta}{f_s} - 2\beta' (1 + 6\alpha) (1 - \delta) \right) \quad (7)$$

where  $w_i^0$  is the nominal mass fraction,  $w_i^{s*}$  is the interfacial solid mass fraction at a given  $f_s$ ,  $k_i$  is the partition coefficient for the solute  $i$ , and:

$$\delta = \exp\left(-\frac{1 - f_s}{2\beta' f_s}\right). \quad (8)$$

Note that Equation (4) has corrected a typo found in Equation (14), published in Reference [35]. In order to solve Equation (7), the initial solid composition  $w_i^s(f_s \rightarrow 0)$  must be determined. This initial solid composition actually corresponds to the dendrite tip composition.

#### 4.2. Tip Undercooling

To establish the dendrite tip composition, the tip operating point must be determined by ascertaining the dendrite tip undercooling:

$$\Delta T = \Delta T_T + \Delta T_R + \Delta T_C + \Delta T_k \quad (9)$$

where  $\Delta T_T$  is the thermal undercooling,  $\Delta T_R$  is the curvature undercooling,  $\Delta T_C$  is the chemical or solutal undercooling, and  $\Delta T_k$  the kinetic undercooling. In the processing conditions considered in this paper,  $\Delta T_T$  and  $\Delta T_k$  were neglected. The curvature undercooling is equal to  $\Gamma/r$  where  $\Gamma$  is the Gibbs–Thomson coefficient and  $r$  is the dendrite tip radius. The determination of the chemical undercooling can be achieved using the well-known KGT model [33]. In this work, to account for fluid flow that can be significant in the GTAW process, a modified formulation of the KGT model derived by Appolaire et al. was chosen [34]. The KGT model considers an isolated dendrite with a tip described by a circular paraboloid. At the interface, the liquid composition  $w_i^*$  is assumed to be homogeneous along the surface of the paraboloid, and at infinity from the nominal solute composition  $w_0$ . Accounting for fluid flow, the supersaturation for each solute  $i$   $\Omega_i = (w_i^{l*} - w_i^0) / (w_i^{l*} (1 - k_i))$  is related to two Péclet numbers: (i) the solutal Péclet number  $P_i = rV/2D_i^l$  and the flow Péclet number  $P_{u_i} = rU/2D_i^l$ , where  $U$  the relative velocity between solid and liquid:

$$\Omega_i = \mathcal{F}(P_i, P_{u_i}). \quad (10)$$

For the range of tip radii and fluid flow velocities encountered in this work, the Stokes regime was considered appropriate [55], and thus function  $\mathcal{F}$  could be given by:

$$\mathcal{F}(P_i, P_{u_i}) = 2P_i \int_1^\infty \exp\{-\ln \eta + (1 - \eta^2)P_i - 2P_{u_i}/E_1(Re_i)[1 - \eta^2 + (1 - \eta^2) \ln \eta] - 2\epsilon P_i \ln \eta\} d\eta \quad (11)$$



where  $\eta$  is the coordinate in the paraboloid frame. The surface of the tip is located at  $\eta = 1$ .  $Re_i = (P_i + P_{u_i})/Sc_i$ ;  $Sc_i$  is the Schmidt number of the solute  $i$ , found by the equation  $Sc_i = \nu/D_i^l$ , where  $\nu$  is the kinematic viscosity of the liquid; and  $\varepsilon$  is the relative density difference between the solid and liquid phases,  $\varepsilon = (\rho_s/\rho_l) - 1$ . This term plays an insignificant role on the supersaturation, and so it was neglected here. The chemical undercooling is then related to the interfacial mass fractions:

$$\Delta T_C = m(w_i^0 - w_i^{l*}) \quad (12)$$

where  $m$  is the liquidus slope of the element. The final expression for the total undercooling becomes:

$$\Delta T = \frac{\Gamma}{r} + \sum_i w_i^0 m_i \left[ 1 - \frac{1}{1 - (1 - k_i)\mathcal{F}(P_i, P_{u_i})} \right] \quad (13)$$

and the associated value of  $w_i^s(f_s \rightarrow 0)$  is:

$$w_i^s(f_s \rightarrow 0) = \frac{k_i w_i^0}{1 - (1 - k_i)\mathcal{F}(P_i, P_{u_i})} \quad (14)$$

$$w_i^s(f_s \rightarrow 0) = \frac{1 + 2\beta'}{1 + \frac{2\beta'}{k}} \times w_i^0. \quad (15)$$

By coupling Equation (15) from Reference [35] with Equation (11) from this work, the following expression of  $\sigma$  was obtained for each solute  $i$ :

$$\sigma_i = \frac{1}{\beta} \left( \frac{1 - \mathcal{F}(P_i, P_{u_i})}{2\mathcal{F}(P_i, P_{u_i})} \right) \quad (16)$$

The obtained value for  $\sigma_i$  was then used to determine  $\beta'$  and thus Equation (7) was solved, giving the evolution of the solute mass fraction for solid fractions ranging from 0 to 1.

#### 4.3. Consequence of Convection on Microsegregation

Gabathuler and Weinberg [56] showed that fluid flow does not penetrate the dendritic skeleton above  $f_s > 0.2$ , while Appolaire et al. [55] showed that fluid flow led to a faster increase of the solid fraction at low solid fractions. At higher solid fractions, the flow is assumed to be described by Darcy's equation, which relates the flow velocity to the pressure gradient in the mushy zone. Defining the local convection time in the mushy zone as  $t_{conv} = 2\lambda_2/U_{MZ}$ , where  $U_{MZ}$  is the flow velocity in the mushy zone, it can be compared to the local solidification time,  $t_f$ , to determine whether or not the flow has an impact on microsegregation. In the present work  $t_f \ll t_{conv}$  for all the investigated processing conditions. It should be noted that this would be different in the case where cellular solidification occurs, as this would involve a change in the characteristic length from the secondary dendrite arm spacing to the primary dendrite arm spacing, and a sharp increase in the permeability. In this case, it is assumed that convection will not affect the microsegregation, except for the initial solid composition.

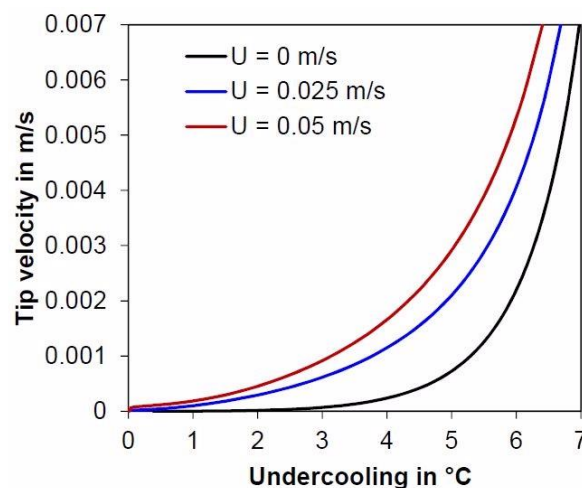
#### 4.4. Evaluation of Tip Undercooling in the Presence of Convection

Table 5 shows the data used for the calculations, wherein a ternary Ni-Cr-Fe alloy was considered and the liquidus and solidus planes were linearized [33]. The Gibbs–Thompson coefficient was approximated with the equation of Magnin and Trivedi [57]. The diffusion coefficients in the liquid were evaluated using the Stokes–Einstein relation. The dynamic viscosity was given by Reference [58]. The Thermo-Calc software, in conjunction with the TTNi8 database, were used to determine the phase equilibrium data. The latent heat of fusion was obtained experimentally by DTA. The value we obtained was close to that used in Reference [40].

**Table 5.** Physical and thermodynamic data used for the calculations.

Physical Quantities	
Gibbs-Thompson coefficient (Km)	$\Gamma = 1.82 \times 10^{-7}$
Diffusion Coefficient for Fe and Cr in molten nickel ( $\text{m}^2/\text{s}$ )	$D_1 = 1.57 \times 10^{-9}$
Heat capacity of liquid ( $\text{J}\cdot\text{kg}^{-1}\cdot\text{K}^{-1}$ ) [59,60]	$C_{p1} = 700$
Thermal conductivity of liquid ( $\text{W}\cdot\text{m}^{-1}\cdot\text{K}^{-1}$ ) [59,61]	$\lambda_1 = 30$
Dynamic viscosity of liquid at 1400 °C ( $\text{N}\cdot\text{s}\cdot\text{m}^{-2}$ ) [58]	$\mu = 0.00483$
Liquid density at $T_1$ ( $\text{kg}\cdot\text{m}^{-3}$ ) [58]	$\rho_1 = 7160$
Latent heat of fusion ( $\text{J}/\text{kg}$ )	$L = 1.3 \times 10^5$
Thermodynamic Quantities	
Liquidus slope for Cr ( $\text{K}\cdot(\%w)^{-1}$ )	$m_{\text{Cr}} = -2.27$
Liquidus slope for Fe ( $\text{K}\cdot(\%w)^{-1}$ )	$m_{\text{Fe}} = 4.55$
Partition coefficient of Cr	$k_{\text{Cr}} = 0.93$
Partition coefficient of Fe	$k_{\text{Fe}} = 1.11$
Composition of Cr in weight percent	29.98
Composition of Fe in weight percent	10.06
Fictive reference temperature in °C [33]	1439.5
Solidus temperature	1409.4
Liquidus temperature	1417.8

Figure 4 shows the undercooling evolution as a function of the tip velocity for different liquid convections. The black line is the classical KGT computation. The blue and red lines are computations with convection in the melt for flow velocities of 0.025 and 0.05 m/s, respectively. These speeds are of the typical order of magnitude for convection at the bottom of the molten bath in GTAW, and can reach several tens of centimeters per second at the surface of the bath [32]. The analyzed region for microsegregation in GTAW is located at the bath bottom, so 0.025 m/s was the value used. For QDS, the convection was considered equal to zero. As can be seen in Figure 4, convection reduces the tip undercooling in GTAW nearer to values encountered in QDS.

**Figure 4.** Undercooling as a function of the tip velocity for several fluid flow intensity convections.

## 5. Comparison between Microsegregation Model and Experimental Results

### 5.1. QDS Experiment

Figure 5 shows the different microsegregation profiles for one QDS experiment, along with the microsegregation predicted by the TB model, lever rule and Scheil rule.

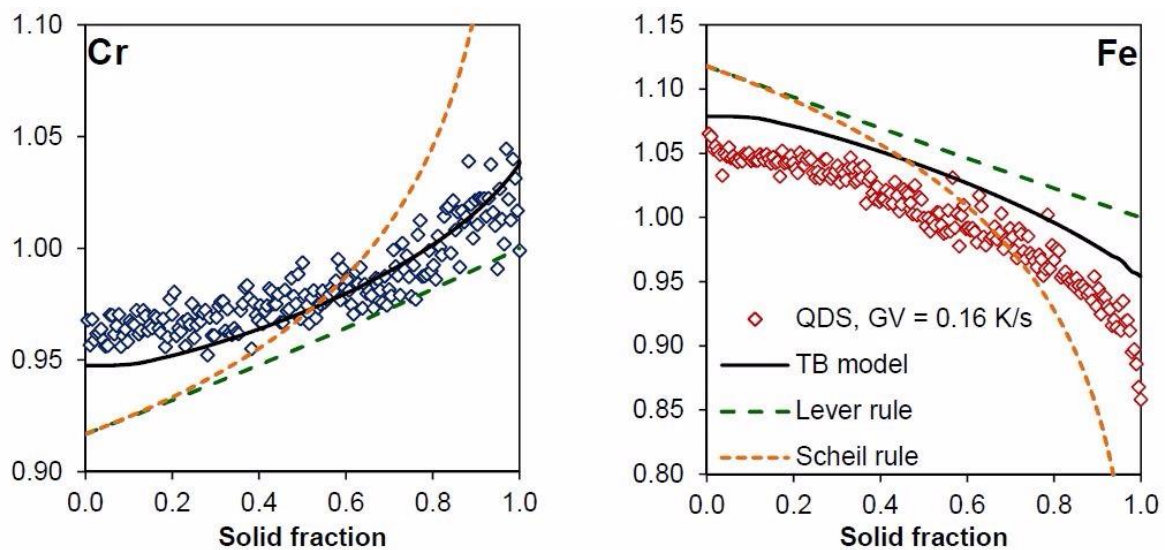


**Figure 5.** Comparison between microsegregation profile and Tong–Beckermann (TB) model for QDS experience for chromium and iron for  $GV = 0.16$  K/s.

The model was able to predict the observed trend at low solid fractions (between 0 and 0.2) in the case of iron, as shown in Figure 5. The trend was less pronounced for chromium, but still present. The importance of taking into account the undercooling, in particular for the small solid fractions (up to 0.3 fs) on the micro-segregation, may be recognized from this data.

The experimental data points and the TB model are slightly shifted apart from one another, in particular for the first solid formed. This could be due to the fact that the TB model computes the composition of solid at the interface with homogenization during the local solidification time. Post homogenization, occurring during subsequent cooling at the dendrite scale, was not taken into account by the model, although it does occur in the experiment. Simplification when computing the data, by assuming the alloy FM52 to be a ternary alloy, was also carried out.

Nevertheless, the curves given by the TB model compare well with the experimental data despite the slight shift previously noted. It should be remembered that the difference between the compositions of the first solid—detected by EPMA and calculated by the TB model—was small. This deviation corresponds to 0.45% and 0.25% by mass, in the case of chromium and iron, respectively. The TB model, coupled with the undercooling calculation, was then validated by the experiments in order to predict the microsegregation profiles.

### 5.2. TB Model and GTAW

Figure 6 shows the Cr and Fe microsegregation profiles for the GTAW experiments, and the microsegregation predicted by the TB model. The Lever and Scheil rule are not shown for the sake of clarity. A good fit between the model and the experiments can be observed, except at high solid fractions. However, the effect of microstructure size should also be considered, not only in the modeling parameters—which take into account back-diffusion and finite liquid diffusion—but also in the experiments, because of the fineness of the microstructures. The EPMA probe smoothed the composition gradient due to the interaction volume of the electrons with the analyzed material. In the case of welding, the interdendritic spacing investigated by the microprobe was SDAS. Following the Castaing relation [62] to determine the depth of penetration of the electron beam, using a classical voltage of 20 kV, a  $0.850 \mu\text{m}$  depth interaction zone was predicted. Generally, 1 micron is often used. Thus, the solid fraction analyzed at each microprobe pointed could be approximated by a  $\frac{\text{depth penetration}}{\text{SDAS}}$  ratio.

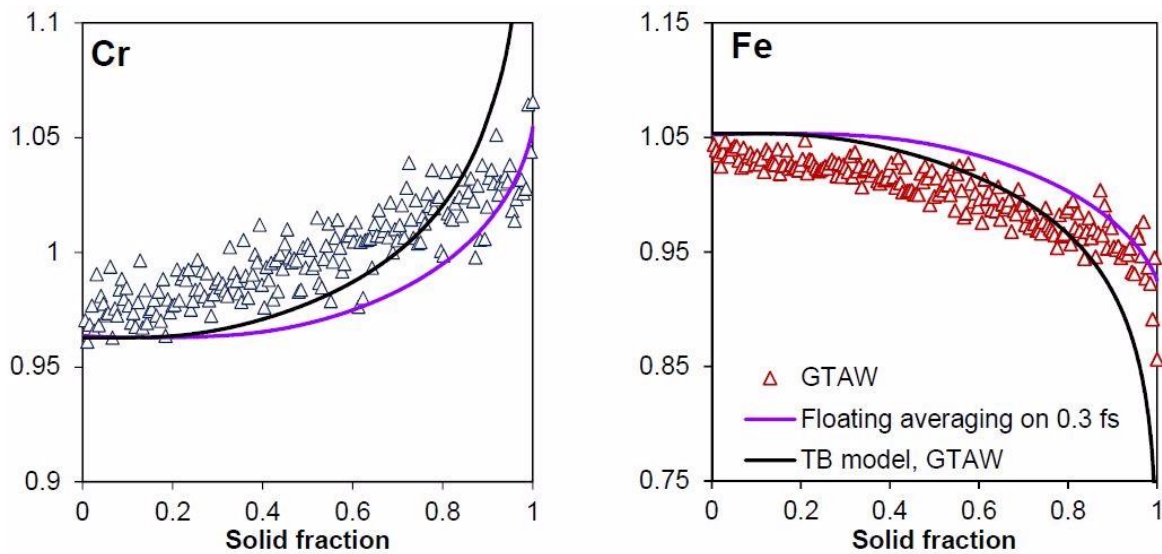


**Figure 6.** Comparison between the microsegregation profiles given by the TB model, and the TB model with floating averaging in the case of the GTAW experiments.

In the case of welding, the SDAS was approximately 3 or 4 microns. Thus, the primary phase solid fraction over this distance must vary from 0 to 1. If the diameter of the microprobe interaction volume is one micron, each analysis point accounts for one third or one quarter of the solid fraction. This must be taken into consideration when comparing the predicted microsegregation profiles to the experimental. In order to do so in this study, a floating average method was used on the model output concentration, ranging from  $\pm 15\%$  solid fraction, for each output point. The results of this method are also plotted in Figure 6.

With the floating average, the TB curves correspond relatively well to the experimental measurements, especially in the case of iron. The slight difference between the microprobe points and the floating averaging TB model is likely caused by the use of the magnitude approximation for the convection in the molten pool.

## 6. Conclusions

The microsegregation behaviors and undercooling of the alloy FM52 were investigated using quenched directional solidification and gas tungsten arc welding. The partition coefficients were confirmed to be close to unity for most alloy elements. Microsegregation was experimentally characterized. Despite the large range of solidification conditions used, it was found that microsegregation does not change drastically. The Tong–Beckerman microsegregation model was then modified to take into account the effect of fluid flow on dendrite tip undercooling. With such modification, the TB model fits well with the experimental data, especially when the interaction volume of the experimental analysis was considered. This modified TB model can be used for microsegregation predictions in all solidification conditions, which, when compared with other analytical models, improves the precision without drastically increasing the complexity.

**Author Contributions:** T.B., D.D., J.Z. and B.R. conceived, designed and carried out the experiments; T.B., D.D. and J.-R.K. wrote and edited the main manuscript. T.B., D.D., B.R., G.T., J.-R.K., V.R. and J.Z. participated in the analysis, discussion and reviewed the manuscript.

**Funding:** This work is included in the MUSICAS (Méthodologie Unifiée de la Simulation pour l'Intégrité et la Contrôlabilité des Assemblages Soudés) multi-partner project. Special thanks to AREVA NP who realized the welding experiences. This work was also supported by the French State through the program "Investment in the future" operated by the National Research Agency (ANR) and referenced by ANR-11-LABX-0008-01 (LabEx DAMAS).

**Acknowledgments:** The assistance of Christine Gendarme (Centre de Compétences Microscopie Electronique Microsonde, CC MEM, Institut Jean Lamour, Parc de Saurupt, 54011, NANCY, FRANCE) for microprobe analysis was greatly appreciated.

**Conflicts of Interest:** The authors declare no conflicts of interest.

## References

1. Suh, J.-H.; Shin, J.-K.; Kang, S.-J.L.; Lim, Y.-S.; Kuk, I.-H.; Kim, J.-S. Investigation of IGSCC behaviour of sensitized and laser surface melted Alloy 600. *Mater. Sci. Eng.* **1998**, *A254*, 67–75. [CrossRef]
2. Kai, J.J.; Liu, M.N. The effects of heat treatment on the carbide evolution and the chromium depletion along grain boundary of Inconel 690 alloy. *Scr. Metall.* **1989**, *23*, 17–22. [CrossRef]
3. Noecker, F.F.; DuPont, J.N. Metallurgical investigation into ductility dip cracking in Ni-based alloys: Part II. *Weld. J.* **2009**, *88*, 62s–77s.
4. Wang, J.D.; Gan, D. Effects of grain boundary carbides on the mechanical properties of Inconel 600. *Mater. Chem. Phys.* **2001**, *70*, 124–128. [CrossRef]
5. Mo, W.; Lu, S.; Li, D.; Li, Y. Effects of filler metal composition on the microstructure and mechanical properties for ERNiCrFe-7multi-pass weldments. *Mater. Sci. Eng. A* **2013**, *582*, 326–337. [CrossRef]
6. Jeng, S.L.; Lee, H.T.; Rehbach, W.P.; Kuo, T.Y.; Weirich, T.E.; Mayer, J.P. Effects of Nb on the microstructure and corrosive property in the Alloy 690–SUS 304L weldment. *Mater. Sci. Eng. A* **2005**, *397*, 229–238. [CrossRef]
7. Ramirez, A.J.; Sowards, J.W.; Lippold, J.C. Improving the ductility-dip cracking resistance of Ni-base alloys. *J. Mater. Process. Technol.* **2006**, *179*, 212–218. [CrossRef]
8. Meng, F.; Wang, J.; Han, E.-H.; Ke, W. The role of TiN inclusions in stress corrosion crack initiation for alloy 690TT in high-temperature and high-pressure water. *Corros. Sci.* **2010**, *52*, 927–932. [CrossRef]
9. Kuo, T.Y.; Lee, H.T. Effects of filler metal composition on joining properties of alloy 690 weldments. *Mater. Sci. Eng. A* **2002**, *338*, 202–212.
10. Crum, J.R.; Gosnay, S.M.; Kiser, S.D.; Zhang, R. Corrosion acceptance testing of weld metals for nuclear service, Materials Selection and Design. *NACE Int.* **2011**, *50*, 70–75.
11. Young, G.A.; Capobianco, T.E.; Penik, M.A.; Morris, B.W.; McGee, J.J. The mechanism of Ductility Dip cracking in Nickel-Chromium Alloys. *Weld. J.* **2008**, *87*, 31s–43s.
12. Collins, M.G.; Lippold, J.C. An investigation of ductility Dip Cracking in Nickel-Based Filler Materials—Part 1. *Weld. J.* **2003**, *82*, 288–295.
13. Collins, M.G.; Ramirez, A.J.; Lippold, J.C. An investigation of ductility Dip Cracking in Nickel-Based Filler Materials—Part 2. *Weld. J.* **2003**, *82*, 348–354.
14. Collins, M.G.; Ramirez, A.J.; Lippold, J.C. An investigation of ductility Dip Cracking in Nickel-Based Filler Materials—Part 3. *Weld. J.* **2004**, *83*, 39–49.
15. Noecker, F.F.; DuPont, J.N. Metallurgical investigation into ductility dip cracking in Ni-based alloys: Part 1. *Weld. J.* **2009**, *8*, 7–20.
16. Nissley, N.E.; Lippold, J.C. Ductility-Dip Cracking Susceptibility of Nickel-Based Weld Metals: Part 1—Strain to Fracture Testing. *Weld. J.* **2008**, *87*, 257–264.
17. Nissley, N.E.; Lippold, J.C. Ductility-Dip Cracking Susceptibility of Nickel-Based Weld Metals: Part 2—Microstructural Characterization. *Weld. J.* **2009**, *88*, 131–140.
18. Kiser, S.D.; Zhang, R.; Baker, B.A. A New Welding Material for Improved resistance to Ductility Dip Cracking. 2008. Available online: <http://www.specialmetalswelding.com/papers/trend%20paper%20-2008.pdf> (accessed on 6 December 2013).
19. INCONEL Filler Metal 52M, Special Metals. Available online: <http://www.specialmetals.com/assets/smc/documents/smw/fm52m.pdf> (accessed on 6 December 2013).
20. INCONEL Filler Metal 52MSS, Special Metals. Available online: <http://www.specialmetals.com/assets/smc/documents/smw/fm52mss.pdf> (accessed on 6 December 2013).
21. Lee, H.T.; Jeng, S.L.; Yen, C.H.; Kuo, T.Y. Dissimilar welding of nickel-based Alloy 690 to SUS 304L with Ti addition. *J. Nucl. Mater.* **2004**, *335*, 59–69. [CrossRef]
22. Ramirez, A.J.; Lippold, J.C. High temperature behaviour of Ni-base weld metal Part II—Insight into the mechanism for ductility deep cracking. *Mater. Sci. Eng. A* **2004**, *380*, 245–258. [CrossRef]



23. Campbell, J.; Tiryakioglu, M. Bifilm defects in Ni-based alloy castings. *Metall. Mater. Trans. B* **2012**, *43*, 902–914. [[CrossRef](#)]
24. Lachowicz, M.; Dudzinski, W.; Haimann, K.; Podrez-Radziszewska, M. Microstructure transformations and cracking in the matrix of  $\gamma$ - $\gamma'$  superalloy Inconel 713C melted with electron beam. *Mater. Sci. Eng. A* **2008**, *479*, 269–276. [[CrossRef](#)]
25. Liu, J.; Duarte, H.P.; Kou, S. Evidence of back diffusion reducing cracking during solidification. *Acta Mater.* **2017**, *122*, 47–59. [[CrossRef](#)]
26. Srikanth, A.; Manikandan, M. Development of welding technique to avoid the sensitization in the alloy 600 by conventional Gas Tungsten Arc Welding method. *J. Manuf. Process.* **2017**, *30*, 452–466. [[CrossRef](#)]
27. Rappaz, M.; Gandin, C.-A.; Desbiolles, J.-L.; Thévoz, P. Prediction of Grain Structures in Various Solidification Processes. *Metall. Mater. Trans. A* **1996**, *27*, 695–705. [[CrossRef](#)]
28. Gandin, C.-A.; Desbiolles, J.L.; Rappaz, M.; Thévoz, P. A Three-Dimensional Cellular Automaton-Finite Element Model for the Prediction of Solidification Grain Structures. *Metall. Mater. Trans. A* **1999**, *30*, 3153–3165. [[CrossRef](#)]
29. Flood, S.C.; Hunt, J.D. Columnar and equiaxed growth I. A model of a columnar front with a temperature dependent velocity. *J. Cryst. Growth* **1987**, *82*, 543–551. [[CrossRef](#)]
30. Chen, S.; Guillemot, G.; Gandin, C.-A. 3D Coupled Cellular Automaton (CA)–Finite Element (FE) Modeling for Solidification Grain Structures in Gas Tungsten Arc Welding (GTAW). *ISIJ Int.* **2014**, *54*, 401–407. [[CrossRef](#)]
31. Krauss, H.G. Experimental Measurement of Thin Plate 304 Stainless Steel GTA Weld Pool Surface Temperatures. *Weld. J.* **1987**, *66*, 353s–359s.
32. Tanaka, M.; Yamamoto, K.; Tashiro, S.; Nakata, K.; Yamamoto, E.; Yamazaki, K.; Suzuki, K.; Murphy, A.B.; Lowke, J.J. Time-dependent calculations of molten pool formation and thermal plasma with metal vapour in gas tungsten arc welding. *J. Phys. D Appl. Phys.* **2010**, *43*, 1–11. [[CrossRef](#)]
33. Kurz, W.; Giovanola, B.; Trivedi, R. Theory of microstructural development during rapid solidification. *Acta Metall.* **1985**, *34*, 823–830. [[CrossRef](#)]
34. Appolaire, B.; Combeau, H.; Lesoult, G. Modeling of equiaxed growth in multicomponent alloys accounting for convection and for the globular/dendritic morphological transition. *Mater. Sci. Eng. A* **2008**, *487*, 33–45. [[CrossRef](#)]
35. Tong, X.; Beckermann, C. A diffusion boundary layer model of microsegregation. *J. Cryst. Growth* **1998**, *187*, 289–302. [[CrossRef](#)]
36. INCONEL Filler Metal 52, Special Metals. Available online: <http://www.specialmetals.com/assets/smc/documents/smw/fm52.pdf> (accessed on 6 December 2013).
37. Boettinger, W.J.; Kattner, U.R. On Differential Thermal Analyzer Curves for the Melting and Freezing of Alloys. *Metall. Mater. Trans. A* **2002**, *33*, 1779–1794. [[CrossRef](#)]
38. Bobadilla, M.; Lacaze, J.; Lesoult, G. Influence des conditions de solidification sur le déroulement de la solidification des aciers inoxydables austénitiques. *J. Cryst. Growth* **1988**, *89*, 531–544. [[CrossRef](#)]
39. Anderson, J.O.; Helander, T.; Höglund, L.; Shi, P.; Sundman, B. Thermo-calc and Dictra, Computation Tools for Materials Science. *Calphad* **2002**, *26*, 273–312. [[CrossRef](#)]
40. Wu, W.; Tsai, C.H. Hot Cracking Susceptibility of Fillers 52 and 82 in Alloy 690 Welding. *Metall. Mater. Trans. A* **1999**, *30*, 417–426. [[CrossRef](#)]
41. Charpentier, M.; Daloz, D.; Hazotte, A.; Gautier, E.; Lesoult, G.; Grange, M. Study of Microstructure and Solute Partitioning in a CastTi-48Al-2Cr-2Nb Alloy by Quenching during Directional Solidification Technique. *Metall. Mater. Trans. A* **2003**, *34*, 2139–2149. [[CrossRef](#)]
42. Zollinger, J.; Lapin, J.; Daloz, D.; Combeau, H. Influence of oxygen on solidification behaviour of cast TiAl-based alloys. *Intermetallics* **2007**, *15*, 1343–1350. [[CrossRef](#)]
43. Lacaze, J.; Lesoult, G. Experimental investigation of the development of microsegregation during solidification of an Al-Cu-Mg-Si aluminium alloy. *Mater. Sci. Eng. A* **1993**, *173*, 119–122. [[CrossRef](#)]
44. Zollinger, J.; Daloz, D. On the sampling methodology to characterize microsegregation. *Mater. Charact.* **2011**, *62*, 1058–1065. [[CrossRef](#)]
45. Blecher, J.J.; Palmer, T.A.; Debroy, T. Solidification Map of a Nickel-Base Alloy. *Metall. Mater. Trans. A* **2014**, *45*, 2142–2151. [[CrossRef](#)]

46. Frenk, A.; Kurz, W. High speed laser cladding: Solidification conditions and microstructure of a cobalt-based alloy. *Mater. Sci. Eng. A* **1993**, *173*, 339–342. [[CrossRef](#)]
47. Dantzig, J.A.; Rappaz, M. *Solidification, Engineering Sciences, Materials*; EPFL Press: Lausanne, Switzerland, 2009.
48. Ganessian, M.; Dye, D.; Lee, P.D. A Technique for characterizing Microsegregation in Multicomponent Alloys and Its Application to Single-Crystal Superalloy Castings. *Metall. Mater. Trans. A* **2005**, *36*, 2191–2204. [[CrossRef](#)]
49. Seo, S.M.; Jeong, H.W.; Ahn, Y.K.; Yun, D.W.; Lee, J.H.; Yoo, Y.S. A comparative study of quantitative microsegregation analyses performed during the solidification of the Ni-base superalloy CMSX-10. *Mater. Charact.* **2014**, *89*, 43–55. [[CrossRef](#)]
50. Liang, Y.-J.; Cheng, X.; Wang, H.-U. A new microsegregation model for rapid solidification condition multicomponent alloys and its application to single-crystal nickel-base superalloys of laser rapid directional solidification. *Acta Materilia* **2016**, *118*, 17–27. [[CrossRef](#)]
51. Scheil, E. Bemerkungen zur Schichtkristallbildung (Retrograde saturation curves). *Z. Metallkunde* **1942**, *34*, 70–72.
52. Clyne, T.W.; Kurz, W. Solute redistribution during solidification with rapid solid state diffusion. *Metall. Trans. A Phys. Metall. Mater. Sci.* **1981**, *12*, 965–971. [[CrossRef](#)]
53. Kobayashi, S. Mathematical analysis of solute redistribution during solidification based in a columnar dendrite model. *Trans. ISIJ Int.* **1988**, *28*, 728–735. [[CrossRef](#)]
54. Wang, C.Y.; Beckermann, C. A unified solute diffusion model for columnar and equiaxed dendritic solidification. *Mater. Sci. Eng. A* **1993**, *171*, 199–211. [[CrossRef](#)]
55. Appolaire, B.; Albert, V.; Combeau, H.; Lesoult, G. Free growth of equiaxed crystals setting in undercooled NH<sub>4</sub>Cl-H<sub>2</sub>O melts. *Acta Mater.* **1998**, *46*, 5851–5862. [[CrossRef](#)]
56. Gabathuler, J.P.; Weinberg, F. Fluid Flow into a dendritic Array under Forced Convection. *Metall. Trans. B* **1983**, *14*, 733–741. [[CrossRef](#)]
57. Magnin, P.; Trivedi, R. Eutectic growth, a modification of the Jackson and Hunt theory. *Acta Metall. Mater.* **1991**, *39*, 453–467. [[CrossRef](#)]
58. Kobatake, H.; Brillo, J. Density and viscosity of ternary Cr-Fe-Ni liquid alloys. *J. Mater. Sci.* **2013**, *48*, 6818–6824. [[CrossRef](#)]
59. Gao, Z.; Ojo, O.A. Modeling analysis of hybrid laser arc welding of single crystal nickel-based superalloys. *Acta Mater.* **2012**, *60*, 3153–3167. [[CrossRef](#)]
60. Bezençon, C. Recouvrement Monocristallin par procédé laser d'un Superalliage à base Nickel. Ph.D. Thesis, Materials science & Eng. Institut, Ecole Polytechnique Fédérale de Lausanne, Lausanne, Switzerland, 2002.
61. Hamouda, H.B. *Modélisation et Simulation de la Structure de Solidification dans les Superalliages Base-Nickel: Application AM1*; Autre; Ecole Nationale Supérieure des Mines de Paris: Paris, France, 2012; NNT: 2012ENMP0040.
62. Castaing, R. *Advances in Electronics and Electron Physics*, 13th ed.; Masson, C., Ed.; Academic Press: New York, NY, USA, 1960; p. 317.

